Chapter 6
Introduction to Radiological Images

Sikander M. Mirza

Contents

6.1 Introduction

Most of imaging modalities in medical science map some spectroscopic property of object onto sensor. The electromagnetic radiations have widely been used for this purpose, and the corresponding imaging modalities use emission, absorption, scattering, or reflection of these radiations. The X-ray radiography, positron emission tomography, fluorescence imaging, and magnetic resonance imaging (MRI) are few examples of the electromagnetic imaging. The electromagnetic spectrum covers a wide range of wavelengths and frequencies as shown in Fig. 6.1.

S.M. Mirza, PhD (✉)
Department of Physics & Applied Mathematics, Pakistan Institute of Engineering & Applied Sciences, Nilore, Islamabad, Pakistan
e-mail: sikander.m.mirza@gmail.com

M. Maqbool (ed.), *An Introduction to Medical Physics*, Biological and Medical Physics, Biomedical Engineering, DOI 10.1007/978-3-319-61540-0_6

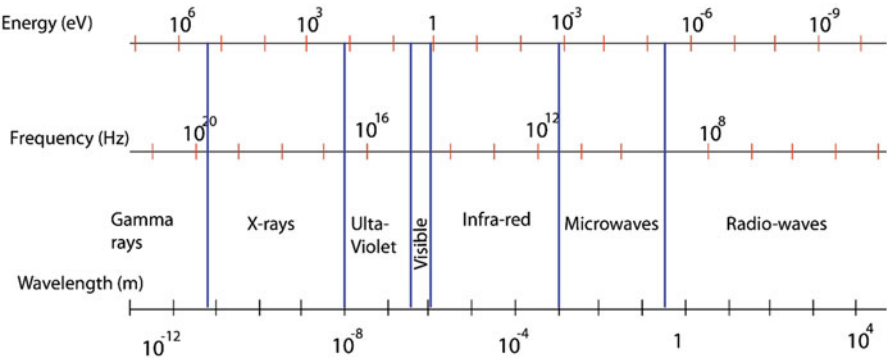

Fig. 6.1 The electromagnetic spectrum in energy, frequency, and wavelength ranges

6.2 X-ray Generator

In clinical environment, X-ray radiographs are obtained using X-ray generator which has X-ray tube at the heart of generation process. It is essentially a vacuum diode valve with an evacuated glass tube containing two electrodes called anode and cathode. The cathode is a filament heated by passage of current, and electrons are released by thermionic emission. These tend to collect around the cathode, forming space charge and inhibiting further emission of electrons. The anode, placed at some distance from cathode, is held at positive potential relative to cathode and attracts these electrons. At low voltage, some of electrons stream out of space charge and reach the anode, while cathode keeps on releasing electrons. Consequently, current is established from cathode to anode. The space charge near the cathode tends to limit the value of this current. As anode voltage is increased, more and more electrons escape the space charge region and tube current increases, while the space charge tends to be depleted. At certain high anode voltage, the space charge disappears altogether, and the tube current reaches maximum value called the "saturation current." The ultimate value of this saturation tube current proportionately depends on the filament heating and in turn on the filament heating current.

The electrons are accelerated as they move from cathode to anode gaining kinetic energy. Just before hitting anode, they have maximum value of kinetic energy (K.E.):

$$\text{K.E.} = \frac{1}{2}mv^2 = eV, \tag{6.1}$$

where m is the mass of electron, v is the speed of electron just before hitting the anode, e is the value of electronic charge, and V is the anode voltage which is typically in tens of keV range. For example, in case of mammography, the value of V is around 30 keV; for chest X-ray, it is around 70 keV; and for skull X-ray,

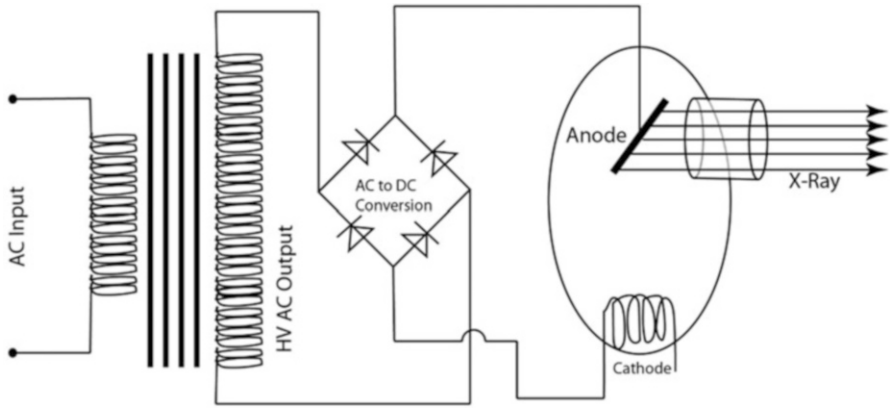

Fig. 6.2 A circuit diagram of a typical X-ray generator highlighting the step-up transformer, the rectifier, and the X-ray tube

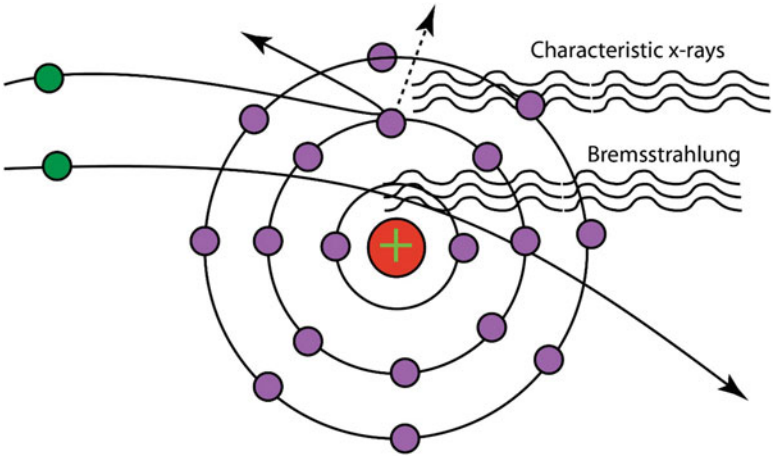

Fig. 6.3 Electrons hitting the anode region can possibly emit Bremsstrahlung or lead to emission of characteristic X-rays by ionizing the anode atoms

120 *keV* is needed. A simplified circuit diagram for a typical X-ray generator is shown in Fig. 6.2.

The electron undergoes abrupt deceleration as it hits the anode material and emits *Bremsstrahlung* (German word for "breaking radiations"). These form a continuous spectrum with maximum energy equal to the kinetic energy of electron hitting the anode. Some of these electrons hit the anode atoms and ionize them which subsequently deionize and emit characteristic X-rays with discrete lines in spectrum. Both of these processes are shown schematically in Fig. 6.3.

For typical X-ray machine, the Bremsstrahlung emission dominates the emitted X-ray intensity, while the fraction emitted as characteristic X-rays is relatively

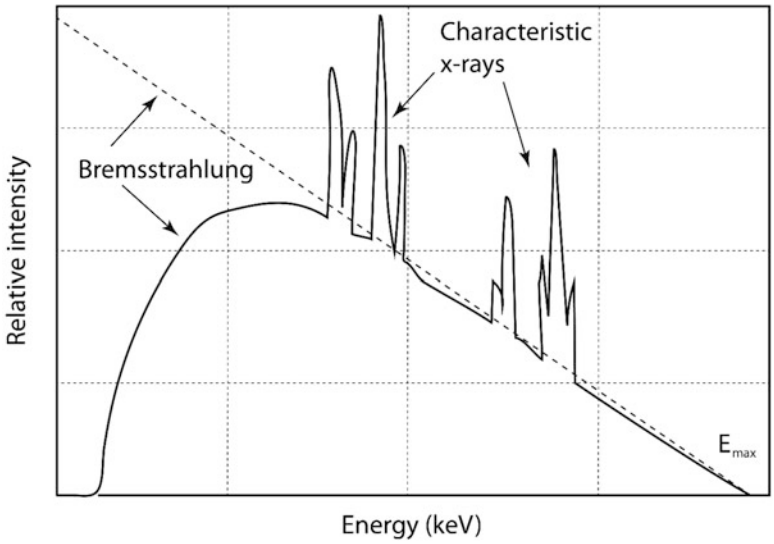

Fig. 6.4 Sketch of a typical emitted X-ray spectrum indicating the relative strengths of Bremsstrahlung and characteristic X-rays

small. For normal diagnostic radiology and for therapy, Bremsstrahlung kind of X-rays is well suited. However, for special applications, in relatively small number of cases, the characteristic X-rays find their use. The emitted X-ray spectrum from a typical X-ray machine is sketched in Fig. 6.4.

6.3 Attenuation

6.3.1 Major Types of Interactions

Incident beam of X-rays interacts with the matter placed in its path via photoelectric effect and Compton scattering. For low-energy X-rays, photoelectric effect dominates, while Compton scattering prevails in the remaining cases. When the energy of X-rays or gamma-rays is higher than threshold value of 1.022 *MeV*, pair production also becomes feasible (Fig. 6.5).

As the result of these interactions, the intensity ($I(x) \equiv$# of photons passing per unit area per unit time) of incident beam decreases, and after penetration Δx distance, it decreases by amount ΔI such that

$$\Delta I \propto -I \times \Delta x, \tag{6.2}$$

and by using μ (attenuation coefficient) as constant of proportionality, we get

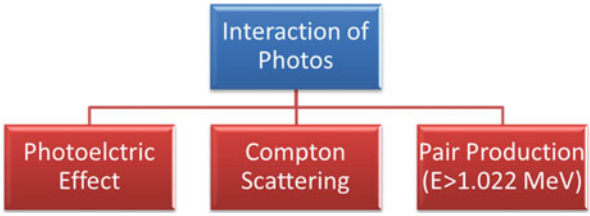

Fig. 6.5 Dominant interaction of X-ray and gamma-ray photons with matter

$$\Delta I = -\mu\, I\, \Delta x, \tag{6.3}$$

which, after integration, yields

$$I(x) = I_0 \exp(-\mu x). \tag{6.4}$$

Starting with incident intensity I_0, the intensity decreases exponentially. Denser materials as well as large thicknesses of materials tend to yield larger decrease in the intensity. While passing through the body, photons get predominantly absorbed in bones while they get transmitted up to some extent while passing through the normal tissue. Consequently, a map of anatomy is projected onto radiographic film or sensitive detector, and a radiographic image is formed.

6.3.2 *Half-Value Layer and Tenth-Value Layer*

Thickness of material attenuating the incident intensity to half of its original value is called half-value layer (HVL), while thickness needed to reduce it to one-tenth of the original value is called tenth-value layer (TVL). Mathematically,

$$\begin{aligned} I = \frac{I_0}{2} &= I_0 \times \exp(-\mu \times \mathrm{HVL}), \\ \Rightarrow \mathrm{HVL} &= \ln(2)/\mu \end{aligned} \tag{6.5}$$

and similarly,

$$\mathrm{TVL} = \frac{\ln(10)}{\mu}. \tag{6.6}$$

We note that a small value of attenuation coefficient implies larger corresponding values of the HVL and TVL.

Solved Example
Statement: Find the HVL and TVL for Al and Cu used as filters in X-ray machines for 80 keV X-rays.

Solution:
Using the Nowotny's "XMuDat" program available freely from the Internet, we find the value of attenuation coefficients:

Material	$\mu/\rho\left(\frac{\text{cm}^2}{\text{gm}}\right)$	$\rho\left(\frac{\text{gm}}{\text{cm}^3}\right)$	Attenuation coefficient (μ, cm^{-1}) at 80 keV
Al	0.2018	2.7	0.54486
Cu	0.7631	8.96	6.83737

Using these data, we get:

Material	HVL (cm)	TVL (cm)
Al	1.272	4.226
Cu	0.1013	0.3367

Due to a larger value of the attenuation coefficient, copper exhibits smaller values of HVL and TVL as compared with the corresponding data for aluminum.

6.4 Collimators

For medical imaging, divergent beams of X-rays must be restricted in order to limit over a desired field of view (FOV). This is achieved with the help of collimators. Additionally, the use of collimator results in a smaller value of patient dose, and also, it tends to reduce the effect of multiple Compton scattered X-ray photons, and consequently, image quality is also improved.

Physically, collimator is generally made of lead or similar high "Z" substance having considerably large value of attenuation coefficient. In simplest configuration, it is composed of two "L-shaped" segments which can slide while placed as a camera aperture. The opening is at some distance from the X-ray "focus," and thereby, a rectangular cone of X-rays is formed defining the FOV at the patient plane. The size of this cone and of the resulting FOV can be adjusted by sliding the "L-shaped" segments of collimator relative to each other.

Such simple arrangements suffer from gradual decrease of X-ray intensity to complete blackness called the penumbra region which is considered unwanted. More complex collimators are designed to overcome such issues.

6.5 Anti-scatter Grids

Due to substantial thickness of the patient body, normally, the X-rays undergo multiple scatterings before getting registered at the radiographic plate. The scattered light results in a decreased value of image contrast and loss of image sharpening which is highly desirable for some situations including heart vein blockage where precise, well-defined boundaries are needed. The anti-scatter

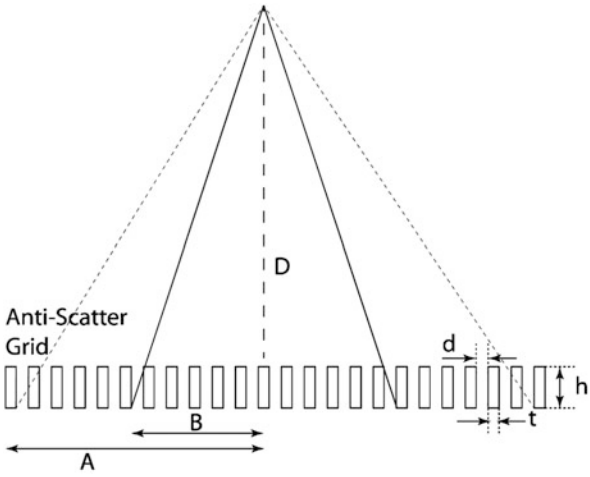

Fig. 6.6 One-dimensional view of the anti-scatter grid indicating the dimensions of lead foils and their mutual separation

grids are used in such cases. These grids are made of lead foils suspended in place by aluminum. The spacing between grid foils is adjusted in order to minimize the passage of scattered X-rays. Let us assume that lead foils of thickness "*t*" each having height "*h*" are separated from each other by distance "*d*" as shown in Fig. 6.6. Then, one can define two following properties of grid:

Grid ratio (GR)

$$\mathrm{GR} = \frac{h}{d}. \tag{6.7}$$

Strip line density (SLD)

$$\mathrm{SLD} = \frac{1}{d+t}. \tag{6.8}$$

The grid ratio is representative of the angle restriction for multiple scattered light control, while the strip line density is indicative of the transparency of the grid itself toward X-rays. As the value of "*d*" (and/or "*t*") is increased, the value of SLD decreases, and at the same time, the value of transparency also decreases.

It is also clear from this figure that for source-to-detector distance (SDD) equal to "*D*," the X-rays can reach up to a critical horizontal distance "*B*" beyond which the shadow of lead foil covers the entire distance "*t*." Using trigonometry, we have

$$\frac{t}{h} = \frac{B}{D}. \tag{6.9}$$

In order to increase the value of distance "*B*" for a broader FOV, the value of SDD must also be increased which entails longer exposure time and the corresponding loss of image quality due to image blur. Another possibility is to

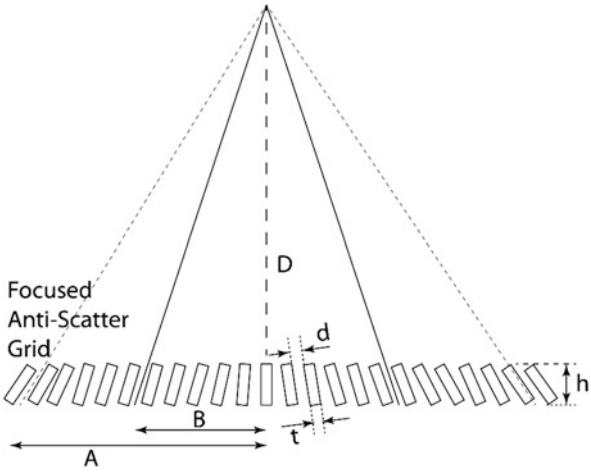

Fig. 6.7 One-dimensional view of the focused anti-scatter grid indicating the dimensions of lead foils and their mutual separation

increase the ratio "t/h" which can be achieved either by increasing the value of "t" or by decreasing the value of "h". Both of them lead to attaining a grid with higher transparency and, at the same time, a grid which allows a higher number of multiply scattered photons thereby killing the original objective for the anti-scatter grids.

The solution to this problem is the use of "focused" grids which have all lead foils aligned to the "focus" as shown in Fig. 6.7.

6.6 Screens

Radiographic film normally used in diagnostic imaging is usually quite thin and consequently does not absorb much of X-rays transmitted by the object. In order to increase their sensitivity, screens are used. These contain scintillation material which converts invisible X-ray photons to multiple numbers of visible range photons. The screens multiply the number of photons while converting them to visible range where the radiographic film sensitivity is high. This double action of screens increases the sensitivity of system by 50-fold typically (Fig. 6.8).

It may also be noted that at low photon count, even the small statistical noise becomes important, while at high photon counts, it becomes insignificant. The screens improve "signal-to-noise ratio" (SNR). One defines the *quantum detection efficiency (QDE)* as the fraction of incident X-ray photons that are absorbed by the screen:

$$\text{QDE} = \frac{\text{No. of photons absorbed in screen}}{\text{Total number of photons incident on screen}}. \tag{6.10}$$

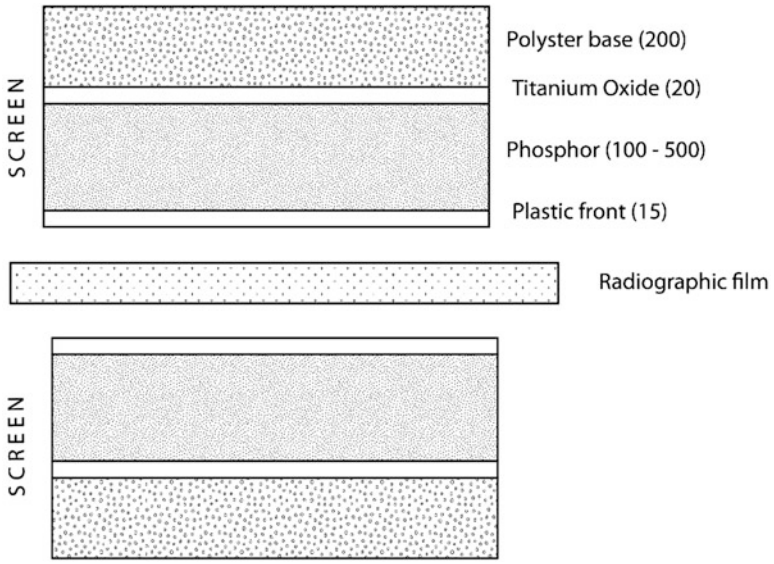

Fig. 6.8 Structural details of typical screen used in radiography (all indicated dimensions are in μm)

The ratio of the number of visible photons absorbed in the film to the number of visible photons emitted by the screen is called the *conversion efficiency (CE)*:

$$\mathrm{CE} = \frac{\text{Number of visible photon absorbed in the film}}{\text{Total number of visible photon emitted by screen}}. \tag{6.11}$$

The overall value of screen efficiency (SE) is the product of the two (Fig. 6.9):

$$\mathrm{SE} = \mathrm{QDE} \times \mathrm{CE}. \tag{6.12}$$

The above figure clearly shows a decreasing trend with increasing X-ray energy for all screen scintillators. The degree of darkness of image on film is quantified by *optical density (OD)* which relates to the corresponding value of *transmittance (T)* such that

$$\mathrm{OD} = \log(1/T). \tag{6.13}$$

A film with 0 value of optical density has 100% transmittance through it, while OD values 1, 2, and 3 have "good exposure," "lung-field," and "very dark" categories correspondingly. A film with OD = 3.5 has maximum possible radiographic darkness.

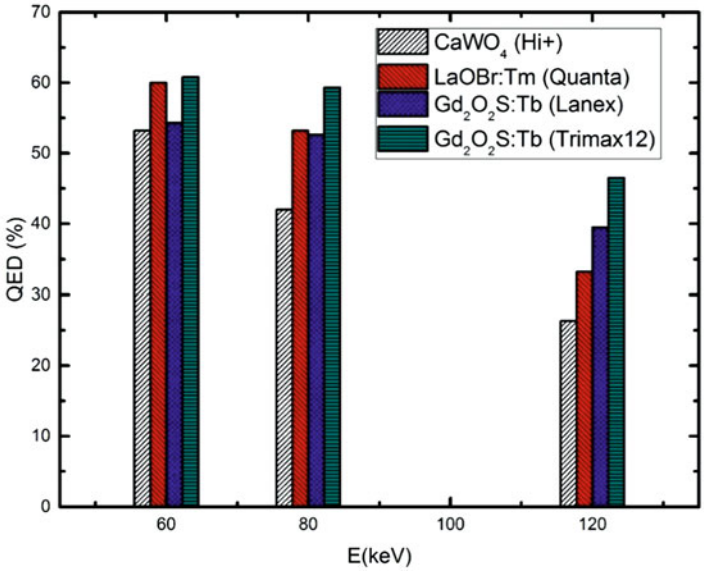

Fig. 6.9 Variation of QED with X-ray energy and type of screen scintillator

6.7 Photo-stimulable Phosphor (PSP)

A class of X-ray scintillators has delayed emission of visible light. It absorbs in incident X-rays in metastable states such that energy becomes stored for a suitable long period of time after the exposure. These metastable states are "read" by stimulus such as laser photons. Many photoluminescence materials exist in nature including ZnS natural diamond, various oxides of silica, and alkali-halides. After exposure to X-rays, sheets of these materials (called image plates, IP for short) store the X-ray energy in the form of latent image which is "read" using laser beam later.

The PSP remains applicable for a wide range of exposure conditions. Consequently, the "retake" frequency of radiographs becomes hugely low.

The image plate is typically barium-fluoro-halide which works as storage medium. The exposure to X-rays leads to the formation of a latent image in the form of electrons trapped in higher energy levels just below conduction band. These electrons can remain trapped in these sites for considerably long times in normal conditions. At reading stage, 633 nm exciting laser beam is used which excites the trapped electrons back to conduction band which subsequently fall to the lower energy levels emitting 390 nm light. The intensity of this visible light is proportional to the incident X-ray intensity for each "pixel." After reading the image plate with laser, the IP is illuminated with light to erase it completely. In this manner, the IP can be reused a large number of times typically exceeding 50,000 cycles.

In the case of PSPs, the workflow does not require any "dark room" or "film processing" delays. Instead, the PSPs are "read" quickly, and instead of a person

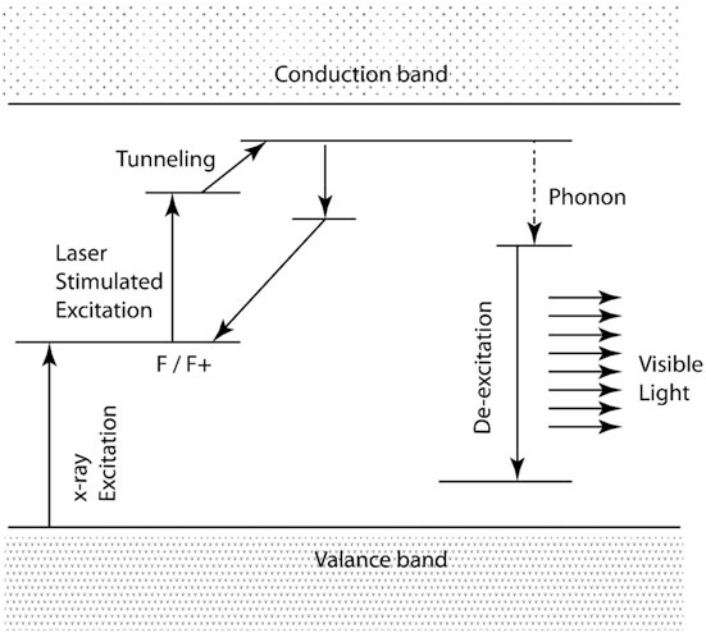

Fig. 6.10 Energy level diagram for excitation through X-ray absorption and subsequent "reading" using laser stimulation (Source: AAPM Report No. 93, 2006)

delivering the processed radiograph to the radiologist, the digital image data is sent instantaneously and, also, saved to permanent storage devices. Note that in conventional radiography, the film is the first thing, while in PSPs, the film storage is the last step (Fig. 6.10).

The detective quantum efficiency (DQE) of PSP is given by the following relation:

$$\mathrm{DQE_{PSP}} = F_{\mathrm{abs}} / \left[(1 + \sigma_{\mathrm{E}})(1 + \sigma_{\mathrm{el}})(1 + \sigma_{\mathrm{S}}) + < N_{\mathrm{PMT}} >^{-1} \right], \tag{6.14}$$

where

F_{abs}= fraction of incident number of photons absorbed in PSP
σ_{E} = coefficient of variation of energy absorbed per X-ray photon in PSP
σ_{el} = coefficient of variation of number of trapped electrons for a given X-ray photon energy in PSP
σ_{S} = coefficient of variation of visible light output for a given number of electrons trapped in PSP
$<N_{\mathrm{PMT}}>$ = average number of photoelectrons detected by PMT per incident X-ray photon

Numerical Example

Statement: Determine the value of detective quantum efficiency (DQE) for PSP using the following data: $\sigma_E = 0.15$, $\sigma_{el} = 0.05$, $\sigma_S = 0.8$, $g = 10$, and $F_{abs} = 0.5$ for normal phosphor, while $F_{abs} = 0.26$ for high-resolution phosphor.

Solution:

As $\mathrm{DQE}_{PSP} = F_{abs}/[(1+\sigma_E)(1+\sigma_{el})(1+\sigma_S) + <N_{PMT}>^{-1}]$,

using the given data,

for normal phosphor, $\mathrm{DQE}_{PSP} = 0.5/[(1+0.15)(1+0.05)(1+0.8)+1/10]$,

we have $\boxed{\mathrm{DQE}_{PSP} = 0.2199 \cong 22\%}$ For high-resolution phosphor,

$$\mathrm{DQE}_{PSP} = 0.26/[(1+0.15)(1+0.05)(1+0.8)+1/10],$$

$$\boxed{\Rightarrow \mathrm{DQE} = \frac{0.26}{2.2735} = 0.114 \cong 11.4\%}$$

6.8 Image Quality Measures

The X-ray image quality indicators typically include various quantitative measures including signal-to-noise ratio (SNR), spatial resolution (SR), line spread function (LSF), modulation transfer function (MTF), and contrast-to-noise ratio (CNR). Each of these measures encompasses some particular attribute of image quality and collectively represents diverse nature of information content of X-ray image.

6.8.1 Signal-to-Noise Ratio (SNR)

The ratio of useful information (signal) to the background (noise) called signal-to-noise ratio represents the degree by which the signal is prominent over the noise. The SNR is affected by statistical distribution (quantum mottle) of X-rays recorded and the spatially nonuniform response of the radiographic film. The value of SNR is dominated by quantum mottle. For a radiograph recorded with tube current value "*I*" with exposure time value "*T*", the value of SNR is given by

$$\mathrm{SNR} \propto \sqrt{IT}. \tag{6.15}$$

Furthermore, the value of SNR shows increasing trend with increase in the kV_p value and thickness of phosphor used in the intensifying screen, while a decreasing trend of SNR is observed with increase in patient body thickness, in the degree of X-ray filtration, and in the degree of absorption in anti-scatter grid.

6.8.2 Spatial Resolution

The ability of radiographic film to show two closely spaced objects separately is called spatial resolution (SR). The value of spatial resolution depends on the following factors:

- *Film grain size:* Slow radiographic films having very small grain size show higher value of SR, while fast films are coarse-grained and exhibit lower value of SR.
- *Thickness of intensifying screens:* The value of SR is affected adversely by thickness of intensifying screen as thicker screens have larger value of light spread function which reduces the value of SR.
- *Focal spot size:* Finite size of focal spot also affects SR adversely since it generates penumbra "P" such that

$$P = f \times (D - H)/H, \tag{6.16}$$

where D is the focal spot distance from detector and H is the distance of the patient body from focal spot. Clearly, it is highly desirable to keep focal spot size as low as possible.

- *Image magnification factor:* A higher value of magnification factor $m = D/H$ also leads to decrease in SR value.

If the ith of above factors leads to contribution R_i toward SR, then, the total resolution is given by

$$R = \sqrt{\sum_{i=1}^{4} R_i^2}. \tag{6.17}$$

6.8.3 Point Spread Function (PSF)

A very small object described by function $O(x, y, z)$ casts image $I(x, y, z)$ in some imaging modality. These are related via expression:

$$I(x, y, z) = O(x, y, z) \otimes h(x, y, z), \tag{6.18}$$

where $h(x, y, z)$ is called point spread function (PSF) and the $\otimes$ operator represents convolution. For ideal imaging system, $I(x, y, z) = O(x, y, z)$ and PSF is represented by delta function. However, all practical imaging systems have intrinsic "noise" which tends to introduce blur in the image through various levels including detector (h_{det}), sampling (h_{samp}), reconstruction (h_{rec}), filter (h_{flt}), etc. The total PSF is

$$h_{\text{tot}} = h_{\text{det}} \otimes h_{\text{samp}} \otimes h_{\text{rec}} \otimes h_{\text{flt}}. \tag{6.19}$$

While the individual components of overall PSF may have different mathematical expressions, the overall PSF may well be approximated by a Gaussian profile in one dimension:

$$h(x) = \frac{1}{\sqrt{2\pi}\,\sigma} \exp\left(-(x - x_o)^2/\sigma^2\right), \tag{6.20}$$

where x_o is the mean or average value of x and σ represents the standard deviation given by

$$\sigma \cong \text{FWHM}/2.36, \tag{6.21}$$

with *FWHM* representing the value of full width at half maximum (spread of Gaussian).

6.8.4 Line Spread Function

For a two-dimensional point spread function PSF(x, y), the line spread function LSF (x) is obtained simply by integrating out the other dimension:

$$\text{LSF}(x) = \int \text{PSF}(x, y)dy. \tag{6.22}$$

The determination of the LSF can be carried out by using line phantom which is typically a wire composed of any high Z-number material such as lead, tungsten, etc. Practically, one can measure the edge spread function (ESF) with the help of a plate placed in the path of X-ray beam. Mathematically, it is convolution of the LSF with a step function (Fig. 6.11).

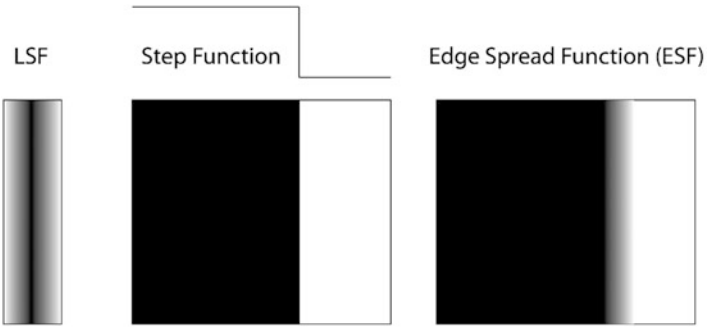

Fig. 6.11 Convolution of LSF with a step function forming the edge spread function

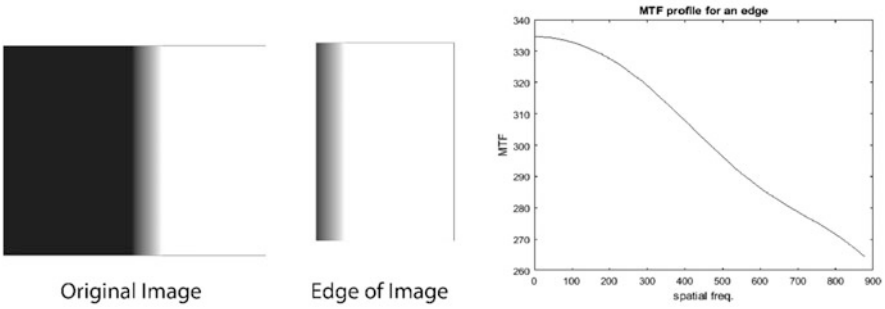

Fig. 6.12 Computed profile of MTF using one-dimensional LSF

6.8.5 Modulation Transfer Function

While the PSF of each component in an imaging system can be quite complicated, taking it from spatial domain to frequency domain makes it easier to combine them. For this purpose, Fourier transform is used:

$$\mathrm{MTF}(k_x, k_y, k_z) = \iiint \mathrm{PSF}(x, y, z)\exp(-j2\pi k_x x)\exp(-j2\pi k_y y)\exp(-j2\pi k_z z) \times dx\, dy\, dz, \tag{6.23}$$

where k_x, k_y, and k_z are spatial frequencies along x, y, and z directions with units cycles/mm or lines/mm (Fig. 6.12). The Matlab code for performing MTF calculations is given below:

```
function getMTF
e=rgb2gray(imread('edge.bmp'));
e=(e); imshow(e(:,2482:end)); figure; %pause;
e=double(e);
esf=e(:,2482);
lsf=gradient(esf);
f=fft(lsf);
mtf=abs(f);
mtf=mtf(1:end/4);
plot(mtf); xlabel('spatial freq.');
ylabel('MTF'); title('MTF profile for an edge');
end
```

6.8.6 *Contrast-to-Noise Ratio*

While the SNR is well established for MRI, the fMRI data does not yield a clear way to use SNR in the same manner. For such type of situations, the use of contrast-to-noise ratio has been proposed. It uses the difference signal in place of signal itself. The image contrast between two regions "A" and "B" is defined as

$$C = (S_A - S_B)/(S_A + S_B), \tag{6.24}$$

where S_A and S_B are image signal intensities in regions "A" and "B," respectively, with "A" as region of interest and "B" as background. The above expression can yield negative values; a better definition could be

$$C = |S_A - S_B|/S_{ref}, \tag{6.25}$$

where S_{ref} represents the value of background signal. For image with a large constant high-intensity offset throughout, the SNR may be high, but a low CNR value will reveal poor image quality.

6.9 Tomographic Projections

The main drawbacks of conventional radiography include its inability to distinguish between objects extended in the direction of X-rays and a high-density material. Both of these may lead to same result on radiographic film. Another drawback is the size of image on the radiographic film which is dependent on the location of the object. If it is closer to focal spot, the image will be larger in size, and if it is closer to the radiographic film, the size becomes closer to its actual size. Both of these limitations are overcome in the tomographic imaging technique. The name "tomo" is derived from Greek where it means a section or a cut. In tomography, projections of X-ray intensity in a perpendicular direction to the viewing direction are used to reconstruct the "density" map of the object as shown in Fig. 6.13.

The collection of projections for various angles $0^o - 180^o$ is called sinogram which is same as the Radon transform of "density" or "μ" profile of the section ("tomo") being studied. The corresponding inverse Radon transform yields the required "density" or "μ" profile. The coordinates (r, s) in the rotated frame are related to the standard coordinates (x, y) as

$$r = x\cos\theta + y\sin\theta, \tag{6.26}$$

$$s = -x\sin\theta + y\cos\theta. \tag{6.27}$$

The Radon transform of the "μ" profile $f(x, y)$ of an object is the collection of ray sums for all angles $\theta \in [0, 180^o]$. If the "abnormality" is in asymmetric position, then the corresponding Radon transform shows a higher value for same set of "r"

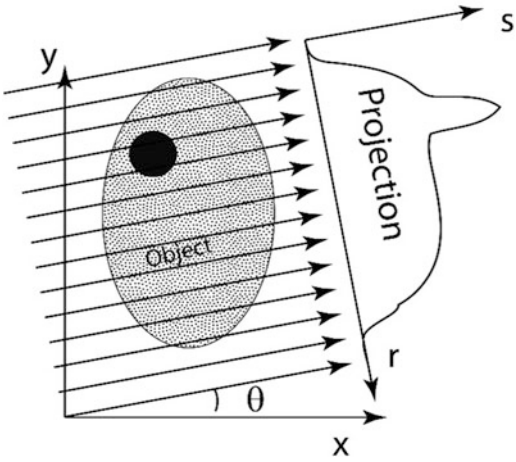

Fig. 6.13 Schematic view of a projection for angle θ of a brain-shaped object containing tumor

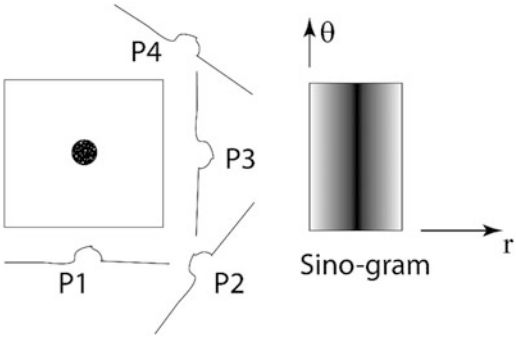

Fig. 6.14 An object with "abnormality" at the center of symmetry along with the corresponding sinogram (Radon transform) of the object

values for all angles. The corresponding data shows symmetric profile in $F(r, s)$ map for all angles as shown in Fig. 6.14.

6.9.1 Image Reconstruction Using Back Projection

Using the sinogram $F(r, s)$, the image reconstruction $f(x, y)$ can be carried out using the simple technique of back projection. In this method, each projection is smeared back onto the pixels by adding the ray-sum values on the previous pixel data. Finally, the data is normalized. This is illustrated in the following example.

Numerical Example
Let us start with a known profile of μ values:

8	3
5	7

The corresponding ray-sum data is shown below:

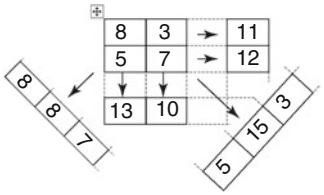

Now, let us start with a blank slate and start back projection by using horizontal direction first:

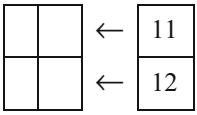

After back projection, the data becomes:

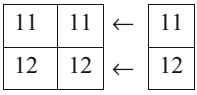

Now, let us project in vertical direction:

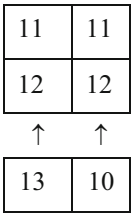

which, after projection, becomes:

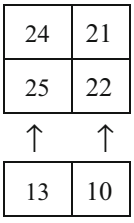

Now, we back project right diagonal data (5,15,3) and it becomes:

39	24
30	37

Finally, we back project the left diagonal data (8,8,7) and it becomes:

47	32
38	44

which, after normalization, becomes:

6.7	4.5
5.4	6.3

which resembles the original (starting data). The results will show improvement if more number of projections are used. The only drawback of this technique is the streaking artifact which arises simply due to smearing of the data back to the region which did not contribute originally. The back projection results in smeared data along the projection direction.

The Shepp-Logan phantom is commonly used for the assessment of the performance of various image reconstruction algorithms (Fig. 6.15). It is a

Fig. 6.15 Image view of Shepp-Logan phantom using Matlab®

mathematically constructed phantom, and as such, it does not have any intrinsic data errors. It represents a section of the skull viewed from the top, and the resulting oval-shaped domain has few "abnormalities" representing tumors. The idea is to check if the reconstructed image is also crisp and clear when compared with the original data. The Matlab code for viewing Shepp-Logan phantom is:

```
P = phantom('Modified Shepp-Logan',200);
imshow(P).
```

For taking the Radon transform (sinogram) of the Shepp-Logan phantom, the following code can be used:

```
function test1
P = phantom('Modified Shepp-Logan',400);
%imshow(P)
theta=[0:180];
[R,xp] = radon(P,theta);
iptsetpref('ImshowAxesVisible','on')
imshow(R,[],'Xdata',theta,'Ydata',xp,...
            'InitialMagnification','fit')
xlabel('\theta (degrees)')
ylabel('x''')
colormap(hot), colorbar
iptsetpref('ImshowAxesVisible','off')
end
```

The resulting image is (Fig. 6.16):

Note the sinusoidal wiggles in the sonogram which are due to nonsymmetric data in the phantom. Now, the projection data (sonogram or Radon-transformed data) needs to be inverted into the original phantom profile. For this purpose, one can use the "iRadon" function in Matlab. If crude steps in angles are used, then the reconstructed image shows streaking artifacts. In the following code, a 10^o step size has been used and the results are shown (Fig. 6.17):

```
function test1
P = phantom('Modified Shepp-Logan',400);
%imshow(P)
theta=[0:10:180];
[R,xp] = radon(P,theta);
subplot(121);imagesc(theta,xp,R); colormap(hot); colorbar
xlabel('\theta'); ylabel('x\prime');

I = iradon(R,10); subplot(122); imshow(I);
end
```

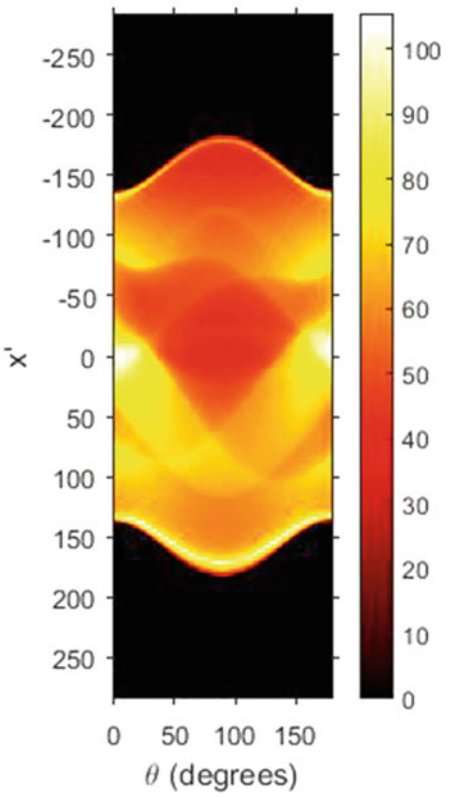

Fig. 6.16 Radon transform of the Shepp-Logan phantom for $\theta \in [0, 180^o]$ range

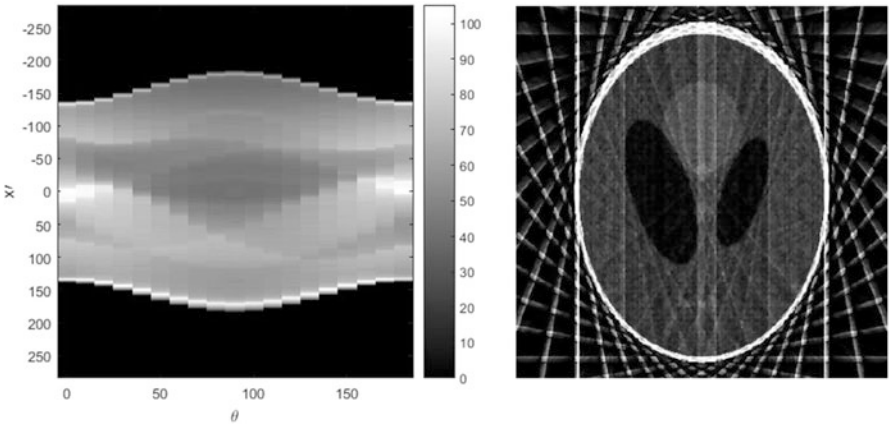

Fig. 6.17 The inverse Radon transform of the Shepp-Logan phantom using crude angular steps ($\Delta\theta = 10^o$)

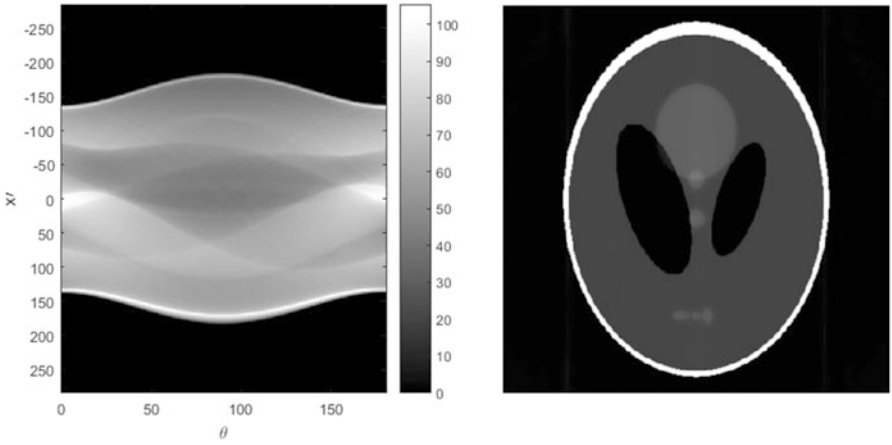

Fig. 6.18 As the angular step size is reduced, the streaking artifacts in the reconstructed image tend to disappear ($\Delta\theta = 1^o$)

For smaller angular steps, the streaking artifacts tend to disappear (Fig. 6.18):

```
function test1
P = phantom('Modified Shepp-Logan',400);
%imshow(P)
theta=[0:1:180];
[R,xp] = radon(P,theta);
subplot(121);imagesc(theta,xp,R); colormap(hot); colorbar
xlabel('\theta'); ylabel('x\prime');

I = iradon(R,1); subplot(122); imshow(I);
end
```

6.9.2 *Filtered Back Projection*

The streaking artifact always affects the reconstructed image. For correction, Ramachandran-Lakshminarayanan (Ram-Lak) proposed a filter which has negative lobes just around the central peak:

$$h(r) = \frac{1}{2dr^2}\left[\sin c\left(\frac{r}{\mathrm{dr}}\right) - \frac{1}{2}\sin c^2\left(\frac{r}{2\mathrm{dr}}\right)\right], \tag{6.28}$$

where dr is sampling interval along r axis. Graphically, we have (Fig. 6.19):

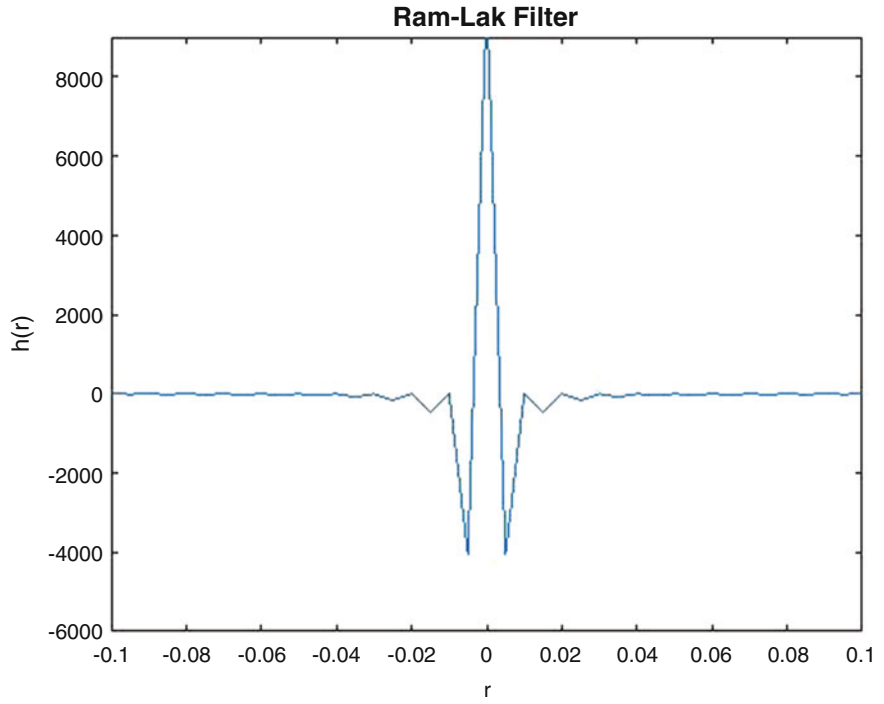

Fig. 6.19 Ram-Lak filter commonly used for removing streaking artifact in the back projection-based image reconstruction

Fig. 6.20 Comparison of reconstructed image without and with Ram-Lak filter

Matlab code for comparing the effect of Ram-Lak filter on reconstructed image and the corresponding output is given below (Fig. 6.20):

```
function test1
P = phantom('Modified Shepp-Logan',400);
%imshow(P)
theta=[0:1:180];
[R,xp] = radon(P,theta);

subplot(131); imshow(P,[]); title('Original');
I = iradon(R,1,'nearest','none'); subplot(132); imshow(I,[]); title('Un-Filtered');
I2 = iradon(R,1,'nearest','Ram-Lak'); subplot(133); imshow(I2,[]); title('Ram-Lak Filtered');
end
```

References

Buhr E, Gnther-Kohfahl S, Neitzel U (2003) Simple method for modulation transfer function determination of digital imaging detectors from edge images. Proc Of SPIE 5030:877–884

Cunningham IA, Reid B (1992) Signal and noise in modulation transfer function determinations using the slit, wire and edge techniques. Med Phys 19:1037–1044

Doyle P, Martin CJ, Gentle D (2006) Application of contrast-to-noise ratio in optimizing beam quality of digital chest radiography: comparison of experimental measurements and theoretical simulations. Phys Med Biol 51:2953–2970

Fujita H, Tsai DY, Itoh T, Doi K, Morishita J, Ueda K, Ohtsuka A (1992) A simple method for determining the modulation transfer function in digital radiography. IEEE Trans Med Imaging 11:34–39

Prabhat P, Arumugam S, Madan VK (2012) Filtering in filtered backprojection computerized tomography. Proc. Natl., Conf. NCNTE-2012 at C.R.I.T., Vashi, Navi Mumbai, 24–25 Feb 2012

Samei E, Flynn MJ (1997) Physical measures of image quality in photostimulable phosphor radiographic systems. SPIE 3032:328–338

Sandborg M, Dance DR, Carlsson GA, Persliden J (1993) The choice of anti-scatter grids in diagnostic radiology: the optimization of image quality and absorbed dose, Dept. of Radiation Physics, Linköping University, US, ISSN 1102–1799

Suetens P (2009) Fundamentals of medical imaging, 2nd edn. Cambridge University Press, Cambridge